

3. Laser Raman Spectroscopy

For many years Raman spectroscopy has been a powerful tool for the investigation of molecular vibrations and rotations. In the pre-laser era, however, its main drawback was a lack of sufficiently intense radiation sources. The introduction of lasers, therefore, has indeed revolutionized this classical field of spectroscopy. Lasers have not only greatly enhanced the sensitivity of spontaneous Raman spectroscopy but they have furthermore initiated new spectroscopic techniques, based on the stimulated Raman effect, such as coherent anti-Stokes Raman scattering (CARS) or hyper-Raman spectroscopy. The research activities in laser Raman spectroscopy have recently shown an impressive expansion and a vast literature on this field is available. In this chapter we summarize only briefly the basic background of the Raman effect and present some experimental techniques that have been developed for Raman spectroscopy of gaseous media. For more thorough studies of this interesting field the textbooks and reviews given in [3.1–3.12] and the conference proceedings [3.13, 3.14] are recommended. More information on Raman spectroscopy of liquids and solids can be found in [3.11, 3.15–3.18].

3.1 Basic Considerations

Raman scattering may be regarded as an inelastic collision of an incident photon $\hbar\omega_i$ with a molecule in the initial energy level E_i (Fig. 3.1a). Following the collision, a photon $\hbar\omega_s$ with lower energy is detected and the molecule is found in a higher-energy level E_f

$$\hbar\omega_i + M(E_i) \rightarrow M^*(E_f) + \hbar\omega_s, \quad \text{with} \quad \hbar(\omega_i - \omega_s) = E_f - E_i > 0. \quad (3.1a)$$

The energy difference $\Delta E = E_f - E_i$ may appear as vibrational, rotational, or electronic energy of the molecule.

If the photon $\hbar\omega_i$ is scattered by a vibrationally excited molecule, it may gain energy and the scattered photon has a higher frequency ω_{as} (Fig. 3.1c), where

$$\hbar\omega_{as} = \hbar\omega_i + E_i - E_f, \quad \text{with} \quad E_i > E_f. \quad (3.1b)$$

This “superelastic” photon scattering is called *anti-Stokes radiation*.

In the energy level scheme (Fig. 3.1b), the intermediate state $E_v = E_i + \hbar\omega_i$ of the system “during” the scattering process is often formally described as

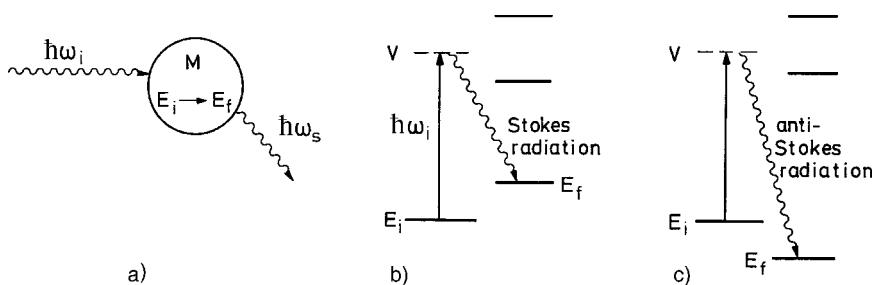


Fig. 3.1a–c. Schematic level diagram of Raman scattering

a *virtual* level, which, however, is not necessarily a “real” stationary eigenstate of the molecule. If the virtual level coincides with one of the molecular eigenstates, one speaks of the *resonance Raman effect*.

A classical description of the *vibrational Raman effect* (which was the main process studied before the introduction of lasers) has been developed by Placek [3.8]. It starts from the relation

$$\mathbf{p} = \boldsymbol{\mu}_0 + \tilde{\alpha}\mathbf{E} , \quad (3.2)$$

between the electric field amplitude $\mathbf{E} = \mathbf{E}_0 \cos \omega t$ of the incident wave and the dipole moment \mathbf{p} of a molecule. The first term $\boldsymbol{\mu}_0$ represents a possible *permanent* dipole moment while $\tilde{\alpha}\mathbf{E}$ is the *induced* dipole moment. The polarizability is generally expressed by the tensor (α_{ij}) of rank two, which depends on the molecular symmetry. Dipole moment and polarizability are functions of the coordinates of the nuclei and electrons. However, as long as the frequency of the incident radiation is far off resonance with electronic or vibrational transitions, the nuclear displacements induced by the polarization of the electron cloud are sufficiently small. Since the electronic charge distribution is determined by the nuclear positions and adjusts “instantaneously” to changes in these positions, we can expand the dipole moment and polarizability into Taylor series in the normal coordinates q_n of the nuclear displacements

$$\begin{aligned} \boldsymbol{\mu} &= \boldsymbol{\mu}(0) + \sum_{n=1}^Q \left(\frac{\partial \boldsymbol{\mu}}{\partial q_n} \right)_0 q_n + \dots , \\ \alpha_{ij}(q) &= \alpha_{ij}(0) + \sum_{n=1}^Q \left(\frac{\partial \alpha_{ij}}{\partial q_n} \right)_0 q_n + \dots , \end{aligned} \quad (3.3)$$

where $Q = 3N - 6$ (or $3N - 5$ for linear molecules) gives the number of normal vibrational modes for a molecule with N nuclei, and $\boldsymbol{\mu}(0) = \boldsymbol{\mu}_0$ and $\alpha_{ij}(0)$ are the dipole moment and the polarizability at the equilibrium configuration $q_n = 0$. For small vibrational amplitudes the normal coordinates $q_n(t)$ of the vibrating molecule can be approximated by

$$q_n(t) = q_{n0} \cos(\omega_n t) , \quad (3.4)$$

where q_{n0} gives the amplitude, and ω_n the vibrational frequency of the n th normal vibration. Inserting (3.4 and 3.3) into (3.2) yields the total dipole moment

$$\begin{aligned} p = \mu_0 + \sum_{n=1}^Q \left(\frac{\partial \mu}{\partial q_n} \right)_0 q_{n0} \cos(\omega_n t) + \alpha_{ij}(0) E_0 \cos(\omega t) \\ + \frac{1}{2} E_0 \sum_{n=1}^Q \left(\frac{\partial \alpha_{ij}}{\partial q_n} \right)_0 q_{n0} [\cos(\omega + \omega_n)t + \cos(\omega - \omega_n)t]. \end{aligned} \quad (3.5)$$

The second term describes the infrared spectrum, the third term the Rayleigh scattering, and the last term represents the Raman scattering. In Fig. 3.2 the dependence of $\partial \mu / \partial q$ and $\partial \alpha / \partial q$ is shown for the three normal vibrations of the CO_2 molecule. This illustrates that $\partial \mu / \partial q \neq 0$ for the bending vibration ν_2 and for the asymmetric stretch ν_3 . These two vibrational modes are called “infrared active.” The polarizability change is $\partial \alpha / \partial q \neq 0$ only for the symmetric stretch ν_1 , which is therefore called “Raman active.”

Since an oscillating dipole moment is a source of new waves generated at each molecule, (3.5) shows that an elastically scattered wave at the frequency ω of the incident wave is produced (Rayleigh scattering) as are inelastically scattered components with the frequencies $\omega - \omega_n$ (*Stokes waves*) and superelastically scattered waves with the frequencies $\omega + \omega_n$ (*anti-Stokes components*). The microscopic contributions from each molecule add up to macroscopic waves with intensities that depend on the population $N(E_i)$ of

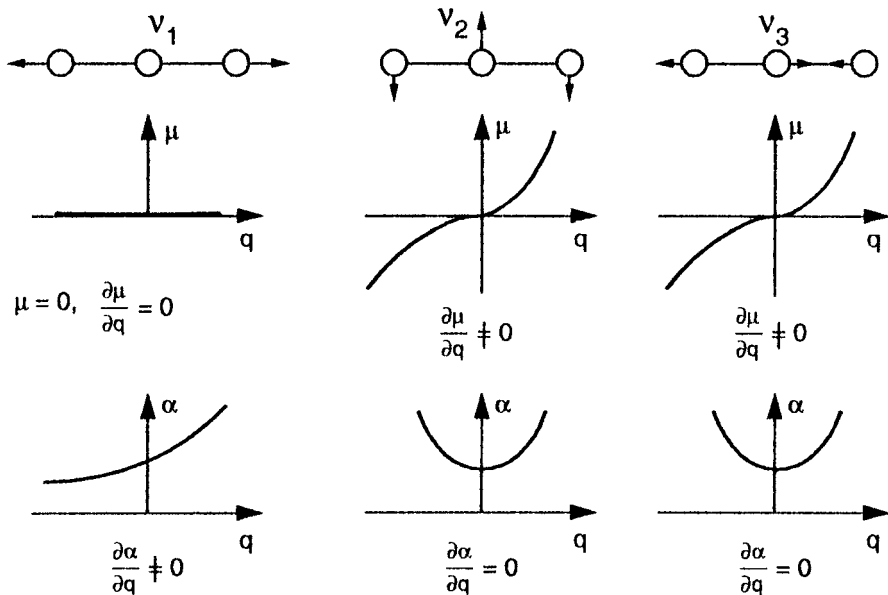


Fig. 3.2. Dependence $\partial \mu / \partial q$ of dipole moment and $\partial \alpha / \partial q$ of polarizability on the normal vibrations of the CO_2 molecule

the molecules in the initial level E_i , on the intensity of the incident radiation, and on the expression $(\partial\alpha_{ij}/\partial q_n)q_n$, which describes the dependence of the polarizability components on the nuclear displacements.

Although the classical theory correctly describes the frequencies $\omega \pm \omega_n$ of the Raman lines, it fails to give the correct intensities and a quantum mechanical treatment is demanded. The expectation value of the component α_{ij} of the polarizability tensor is given by

$$\langle \alpha_{ij} \rangle_{ab} = \int u_b^*(q) \alpha_{ij} u_a(q) dq, \quad (3.6)$$

where the functions $u(q)$ represent the molecular eigenfunctions in the initial level a and the final level b . The integration extends over all nuclear coordinates. This shows that a computation of the intensities of Raman lines is based on the knowledge of the molecular wave functions of the initial and final states. In the case of vibrational-rotational Raman scattering these are the rotational-vibrational eigenfunctions of the electronic ground state.

For small displacements q_n , the molecular potential can be approximated by a harmonic potential, where the coupling between the different normal vibrational modes can be neglected. The functions $u(q)$ are then separable into a product

$$u(q) = \prod_{n=1}^Q w_n(q_n, v_n), \quad (3.7)$$

of vibrational eigenfunction of the n th normal mode with v_n vibrational quanta. Using the orthogonality relation

$$\int w_n w_m dq = \delta_{nm}, \quad (3.8)$$

of the functions $w_n(q_n)$, one obtains from (3.6 and 3.3)

$$\langle \alpha_{ij} \rangle_{ab} = (\alpha_{ij})_0 + \sum_{n=1}^Q \left(\frac{\partial \alpha_{ij}}{\partial q_n} \right)_0 \int w_n(q_n, v_a) q_n w_n(q_n, v_b) dq_n. \quad (3.9)$$

The first term is a constant and is responsible for the Rayleigh scattering. For nondegenerate vibrations the integrals in the second term vanish unless $v_a = v_b \pm 1$. In these cases it has the value $[\frac{1}{2}(v_a + 1)]^{1/2}$ [3.18]. The basic intensity parameter of vibrational Raman spectroscopy is the derivative $(\partial\alpha_{ij}/\partial q)$, which can be determined from the Raman spectra.

The intensity of a Raman line at the Stokes or anti-Stokes frequency $\omega_s = \omega \pm \omega_n$ is determined by the population density $N_i(E_i)$ in the initial level $E_i(v, J)$, by the intensity I_L of the incident pump laser, and by the

Raman scattering cross section $\sigma_R(i \rightarrow f)$ for the Raman transition $E_i \rightarrow E_f$:

$$I_s = N_i(E_i)\sigma_R(i \rightarrow f)I_L. \quad (3.10)$$

At thermal equilibrium the population density $N_i(E_i)$ follows the Boltzmann distribution

$$N_i(E_i, v, J) = \frac{N}{Z} g_i e^{-E_i/kT}, \quad \text{with} \quad N = \sum N_i. \quad (3.11a)$$

The statistical weight factors g_i depend on the vibrational state $v = (n_1 v_1, n_2 v_2, \dots)$, the rotational state with the rotational quantum number J , the projection K onto the symmetry axis in the case of a symmetric top, and furthermore on the nuclear spins I of the N nuclei. The partition function

$$Z = \sum_i g_i e^{-E_i/kT}, \quad (3.11b)$$

is a normalization factor, which makes $\sum N_i(v, J) = N$, as can be verified by inserting (3.11b) into (3.11a).

In case of Stokes radiation the initial state of the molecules may be the vibrational ground state, while for the emission of anti-Stokes lines the molecules must have initial excitation energy. Because of the lower population density in these excited levels, the intensity of the anti-Stokes lines is lower by a factor $\exp(-\hbar\omega_v/kT)$.

Example 3.1.

$\hbar\omega_v = 1000 \text{ cm}^{-1}$, $T = 300 \text{ K} \rightarrow kT \sim 250 \text{ cm}^{-1} \rightarrow \exp(-E_i/kT) \approx e^{-4} \approx 0.018$. With comparable cross sections σ_R the intensity of anti-Stokes lines is therefore lower by two orders of magnitude compared with those of Stokes lines.

The scattering cross section depends on the matrix element (3.9) of the polarizability tensor and furthermore contains the ω^4 frequency dependence derived from the classical theory of light scattering. One obtains [3.19] analogously to the two-photon cross section (Sect. 2.5)

$$\sigma_R(i \rightarrow f) = \frac{8\pi\omega_s^4}{9\hbar c^4} \left| \sum_j \frac{\langle\alpha_{ij}\rangle\hat{\mathbf{e}}_L\langle\alpha_{jf}\rangle\hat{\mathbf{e}}_s}{\omega_{ij} - \omega_L - i\gamma_j} + \frac{\langle\alpha_{ji}\rangle\hat{\mathbf{e}}_L\langle\alpha_{jf}\rangle\hat{\mathbf{e}}_s}{\omega_{jf} - \omega_L - i\gamma_j} \right|^2, \quad (3.12)$$

where $\hat{\mathbf{e}}_L$ and $\hat{\mathbf{e}}_s$ are unit vectors representing the polarization of the incident laser beam and the scattered light. The sum extends over all molecular levels j with homogeneous width γ_j accessible by single-photon transitions from the initial state i . We see from (3.12) that the initial and final states are connected by *two-photon* transitions, which implies that both states have the same parity. For example, the vibrational transitions in homonuclear diatomic molecules, which are forbidden for single-photon infrared transitions, are accessible to Raman transitions.

The matrix elements $\langle \alpha_{ij} \rangle$ depend on the symmetry characteristics of the molecular states. While the theoretical evaluation of the magnitude of $\langle \alpha_{ij} \rangle$ demands a knowledge of the corresponding wave functions, the question whether $\langle \alpha_{ij} \rangle$ is zero or not depends on the symmetry properties of the molecular wave functions for the states $|i\rangle$ and $|f\rangle$ and can therefore be answered by group theory without explicitly calculating the matrix elements (3.9).

According to (3.12), the Raman scattering cross section increases considerably if the laser frequency ω_L matches a transition frequency ω_{ij} of the molecule (resonance Raman effect) [3.20, 3.21]. With tunable dye lasers and optical frequency doubling this resonance condition can often be realized. The enhanced sensitivity of resonant Raman scattering can be utilized for measurements of micro-samples or of very small concentrations of molecules in solutions, where the absorption of the pump wave is small in spite of resonance with a molecular transition.

If the frequency difference $\omega_L - \omega_s$ corresponds to an electronic transition of the molecule, we speak of electronic Raman scattering [3.22, 3.23], which gives complementary information to electronic-absorption spectroscopy. This is because the initial and final states must have the same parity, and therefore a direct dipole-allowed electronic transition $|i\rangle \rightarrow |f\rangle$ is not possible.

In paramagnetic molecules Raman transitions between different fine-structure components (spin-flip Raman transitions) can occur [3.9]. If the molecules are placed in a longitudinal magnetic field parallel to the laser beam, the Raman light is circularly polarized and is measured as σ^+ light for $\Delta M = +1$ and as σ^- for $\Delta M = -1$ transitions.

3.2 Experimental Techniques of Linear Laser Raman Spectroscopy

The scattering cross sections in spontaneous Raman spectroscopy are very small, typically on the order of 10^{-30} cm^2 . The experimental problems of detecting weak signals in the presence of intense background radiation are by no means trivial. The achievable signal-to-noise ratio depends both on the pump intensity and on the sensitivity of the detector. Recent years have brought remarkable progress on the source as well as on the detector side [3.24]. The incident light intensity can be greatly enhanced by using multiple reflection cells, intracavity techniques (Sect. 1.2.2), or a combination of both. Figure 3.3 depicts as an example of such advanced equipment a Raman spectrometer with a multiple-reflection Raman cell inside the resonator of an argon laser. The laser can be tuned by the Brewster prism with reflecting backside (LP + M) to the different laser lines [3.25]. A sophisticated system of mirrors CM collects the scattered light, which is further imaged by the lens L_1 onto the entrance slit S of the spectrometer. A Dove prism DP [3.26] turns the image of the line source by 90° to make it parallel to the entrance slit. Figure 3.4, which shows the pure rotational Raman spectrum of C_2N_2 , illustrates

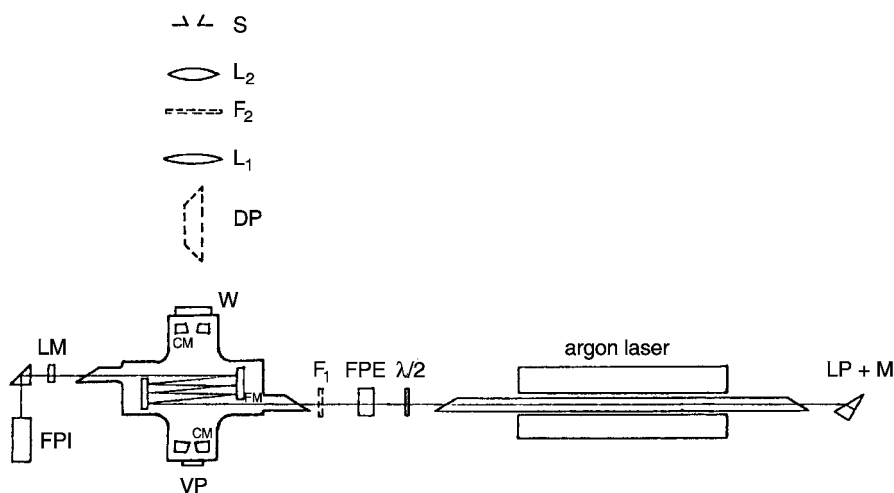


Fig. 3.3. Experimental arrangement for intracavity Raman spectroscopy with an argon laser: CM, multiple reflection four-mirror system for efficient collection of scattered light; LM, laser-resonator mirror; DP, Dove prism, which turns the image of the horizontal interaction plane by 90° in order to match it to the vertical entrance slit S of the spectrograph; FPE, Fabry-Perot etalon to enforce single-mode operation of the argon laser; LP, Littrow prism for line selection [3.25]

the sensitivity that can be obtained with this setup [3.25].

In earlier days of Raman spectroscopy the photographic plate was the only detector used to record the Raman spectra. The introduction of sensitive photomultipliers and, in particular, the development of image intensifiers and optical multichannel analyzers with cooled photocathodes (Vol. 1, Sect. 4.5) have greatly enhanced the detection sensitivity. Image intensifiers and instrumentation such as optical multichannel analyzers (OMAs) or CCD arrays (Vol. 1, Sect. 4.5.3) allow simultaneous recording of extended spectral ranges with sensitivities comparable to those of photomultipliers [3.26].

The third experimental component that has contributed to the further improvement of the quality of Raman spectra is the introduction of digital computers to control the experimental procedure, to calibrate the Raman spec-

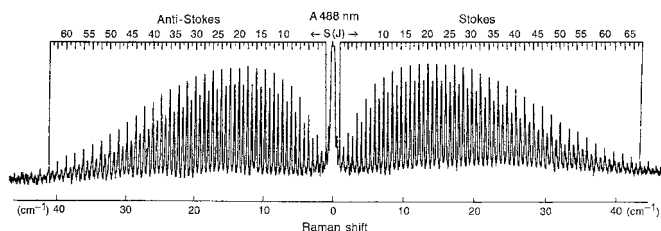


Fig. 3.4. Rotational Raman spectrum of C_2N_2 excited with the 488-nm line of the argon laser in the experimental setup of Fig. 3.3 and recorded on a photographic plate with 10-min exposure time [3.25]

tra, and to analyze the data. This has greatly reduced the time spent for preparing the data for the interpretation of the results [3.27].

Because of the increased sensitivity of an intracavity arrangement, even weak vibrational overtone bands with $\Delta v > 1$ can be recorded with rotational resolution. For illustration, Fig. 3.5 shows the rotationally resolved Q-branch of the D_2 molecule for the transitions ($v' = 2 \leftarrow v'' = 0$) [3.28]. The photon counting rate for the overtone transitions was about 5000 times smaller than those for the fundamental ($v' = 1 \leftarrow v'' = 0$) band. This overtone Raman spectroscopy can also be applied to large molecules, as has been demonstrated for the overtone spectrum of the torsional vibration of CH_3CD_3 and C_2H_6 , where the torsional splittings could be measured up to the 5th torsional level [3.29].

Just as in absorption spectroscopy, the sensitivity may be enhanced by difference laser Raman spectroscopy, where the pump laser passes alternately through a cell containing the sample molecules dissolved in some liquid and through a cell containing only the liquid. The basic advantages of this difference technique are the cancellation of unwanted Raman bands of the solvent in the spectrum of the solution and the accurate determination of small frequency shifts due to interactions with the solvent molecules.

In the case of strongly absorbing Raman samples, the heat production at the focus of the incident laser may become so large that the molecules under investigation may thermally decompose. A solution to this problem is the rotating sample technique [3.30], where the sample is rotated with an angular velocity Ω . If the interaction point with the laser beam is R centimeters away from the axis, the time T spent by the molecules within the focal region with diameter d [cm] is $T = d/(R\Omega)$. This technique which allows much higher input powers and therefore better signal-to-noise ratios,

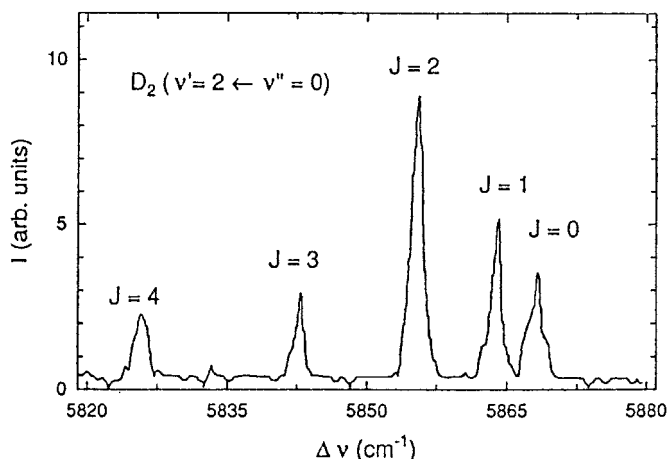


Fig. 3.5. Rotationally resolved Q-branch in the ($v' = 2 \leftarrow v'' = 0$) overtone spectrum of the D_2 molecule, measured with the sample inside the resonator of a 250-W argon laser at $\lambda = 488 \text{ nm}$ [3.28]

can be combined with the difference technique by mounting a cylindrical cell onto the rotation axis. One half of the cell is filled with the liquid Raman sample in solution, the other half is only filled with the solvent (Fig. 3.6).

A larger increase of sensitivity in linear Raman spectroscopy of liquids has been achieved with optical-fiber Raman spectroscopy. This technique uses a capillary optical fiber with the refractive index n_f , filled with a liquid with refractive index $n_e > n_f$. If the incident laser beam is focused into the fiber, the laser light as well as the Raman light is trapped in the core due to internal reflection and therefore travels inside the capillary. With sufficiently long capillaries (1–30 m) and low losses, very high spontaneous Raman intensities can be achieved, which may exceed those of conventional techniques by factors of 10^3 [3.31]. Figure 3.7 shows schematically the experimental arrangement where the fiber is wound on a drum. Because of the increased sensitivity, this fiber technique also allows one to record second- and third-order Raman bands, which facilitates complete assignments of vibrational spectra [3.32].

The sensitivity of Raman spectroscopy in the gas phase can be greatly enhanced by combination with one of the detection techniques discussed

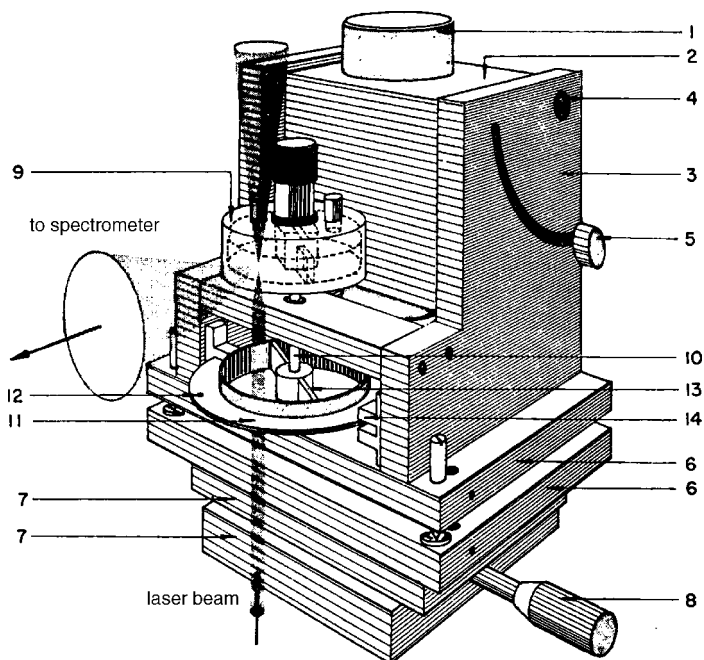


Fig. 3.6. Rotating sample cell used for difference Raman spectroscopy: 1, motor; 2, motor block; 3, side parts; 4, motor axis; 5, set screw; 6, kinematic mount; 7, x - y precision ball glider; 8, adjustment screw; 9, divided liquid cell for difference Raman spectroscopy; 10, axis for trigger wheel; 11, trigger wheel; 12, trigger hole; 13, bar; 14, optoelectronic array consisting of a photodiode and transistor [3.30]

in Chap. 1. For example, the vibrationally excited molecules produced by Raman–Stokes scattering can be selectively detected by resonant two-photon ionization with two visible lasers or by UV ionization with a laser frequency ω_{UV} , which can ionize molecules in level E_f but not in E_i (Fig. 3.8).

The combination of Raman spectroscopy with Fourier-transform spectroscopy [3.33] allows the simultaneous detection of larger spectral ranges in the Raman spectra.

The information obtained from linear Raman spectroscopy is derived from the following experimental data:

- The linewidth of the scattered radiation, which represents for gaseous samples a convolution of the Doppler width, collisional broadening, spectral profile of the exciting laser, and natural linewidth, depending on the lifetimes of molecular levels involved in the Raman transition.

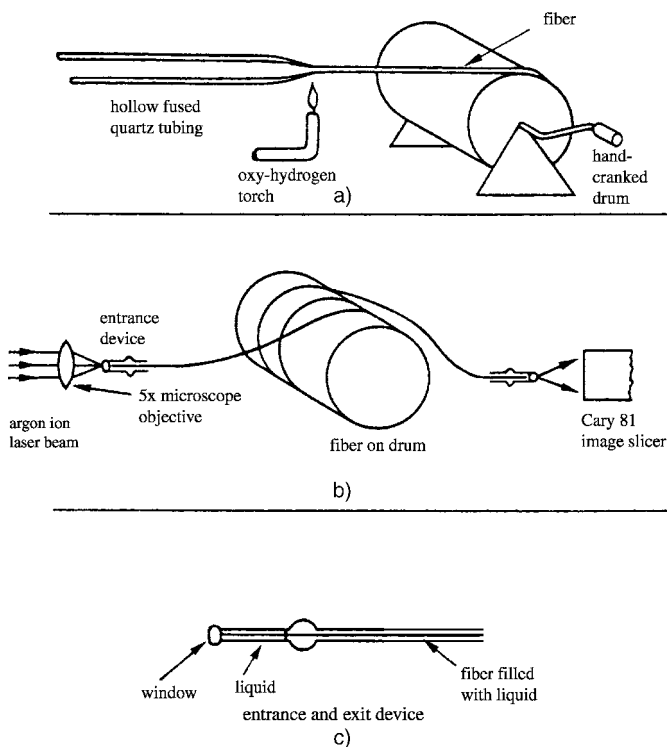


Fig. 3.7a–c. Raman spectroscopy of liquid samples in a thin capillary fiber: (a) production of the fiber; (b) incoupling of an argon laser beam with a microscope objective into the fiber and imaging of the outcoupled radiation into a spectrometer; (c) fiber with liquid [3.30]

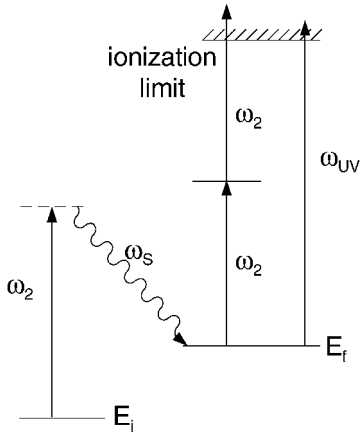


Fig. 3.8. Detection of Raman–Stokes scattering by photoionization of the excited level E_f either by one UV photon ($IP(E_f) < \hbar\omega_{UV} < IP(E_i)$) or by resonant two-photon ionization

- The degree of polarization ρ of the scattered light, defined as

$$\rho = \frac{I_{\parallel} - I_{\perp}}{I_{\parallel} + I_{\perp}}, \quad (3.13)$$

where I_{\parallel} and I_{\perp} are the intensities of the scattered light with a polarization parallel and perpendicular, respectively, to that of a linearly polarized excitation laser. A more detailed calculation shows that for statistically oriented molecules the degree of polarization

$$\rho = \frac{3\beta^2}{45\bar{\alpha}^2 + 4\beta^2}, \quad (3.14)$$

depends on the mean value $\bar{\alpha} = (\alpha_{xx} + \alpha_{yy} + \alpha_{zz})/3$ of the diagonal components of the polarizability tensor $\tilde{\alpha}$ and on the anisotropy

$$\beta^2 = \frac{1}{2} \left[(\alpha_{xx} - \alpha_{yy})^2 + (\alpha_{yy} - \alpha_{zz})^2 + (\alpha_{zz} - \alpha_{xx})^2 + 6(\alpha_{xy}^2 + \alpha_{xz}^2 + \alpha_{zx}^2) \right]. \quad (3.15)$$

Measurements of ρ and β therefore allow the determination of the polarizability tensor [3.34].

It turns out that

$$\begin{aligned} \overline{\alpha_{xx}^2} &= \overline{\alpha_{yy}^2} = \overline{\alpha_{zz}^2} = \frac{1}{45} (45\bar{\alpha}^2 + 4\beta^2), \\ \overline{\alpha_{xy}^2} &= \overline{\alpha_{xz}^2} = \overline{\alpha_{yz}^2} = \frac{1}{15} \beta^2. \end{aligned} \quad (3.16)$$

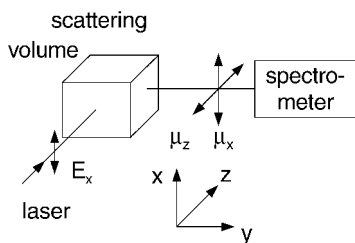


Fig. 3.9. Possible scattering geometry for measurements of the components α_{xx} and α_{zx} of the polarizability tensor

With the experimental arrangement of Fig. 3.9, where the exciting laser is polarized in the x -direction and the Raman light is observed in the y -direction without polarizer ($\mu_x + \mu_z$), the measured intensity becomes

$$I_{x,(x+z)} = \frac{\omega^4 \cdot I_0}{16\pi^2 \epsilon_0^2 c^4} (\alpha_{xx}^2 + \alpha_{zx}^2). \quad (3.17)$$

- The intensity of the Raman lines is proportional to the product of the Raman scattering cross section σ_R , which depends according to (3.12) on the matrix elements $\langle \alpha_{ij} \rangle$ of the polarizability tensor and the density N_i of molecules in the initial state. If the cross sections σ_R have been determined elsewhere, the intensity of the Raman lines can be used for measurements of the population densities $N(v, J)$. Assuming a Boltzmann distribution (3.11a), the temperature T of the sample can be derived from measured values of $N(v, J)$. This is frequently used for the determination of unknown temperature profiles in flames [3.35] or of unknown density profiles in liquid or gaseous flows [3.36] at a known temperature (Sect. 3.5). One example is intracavity Raman spectroscopy of molecules in a supersonic jet, demonstrated by van Helvoort et al. [3.37]. If the intracavity beam waist of an argon-ion laser is shifted to different locations of the molecular jet (Fig. 3.10), the vibrational and rotational temperatures of the molecules (Sect. 4.2) and their local variations can be derived from the Raman spectra.

More details of recent techniques in linear laser Raman spectroscopy can be found in [3.11, 3.38].

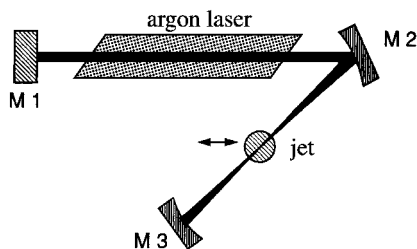


Fig. 3.10. Intracavity Raman spectroscopy of molecules in a cold jet with spatial resolution